Journal of Materials Chemistry C

ROYAL SOCIETY OF CHEMISTRY

COMMUNICATION

View Article Online
View Journal | View Issue

Cite this: J. Mater. Chem. C, 2022, 10, 2544

Received 3rd September 2021,
Accepted 21st October 2021

DOI: 10.1039/d1tc04176b

rsc.li/materials-c

A perylene diimide dimer-based electron transporting material with an A–D–A structure for efficient inverted perovskite solar cells†

Yunhao Fan,‡[a] Fei Wu,‡[b] Fan Liu,‡[a] Mengmeng Han,[a] Kai Chang,[a] Linna Zhu,*[b] Qianqian Li*[a] and Zhen Li*[ac]

Through the introduction of two perylene diimide (PDI) moieties to the triphenylamine (TPA) core, a PDI dimer-based electron transport material has been synthesized with an A (electron acceptor)–D (electron donor)–A structure. It demonstrated a high electron mobility of 8.23 × 10^{-4} cm^2 V^{-1} s^{-1} as a thin film and achieved a PCE of 20.07% in perovskite solar cells, higher than that of $PC_{61}BM$ (18.38%) as the standard reference under the same conditions. This is the highest conversion efficiency among various PDI derivatives as ETMs, providing the optimized molecular configuration by combination of twisted core (TPA) and planar peripheral moieties (PDI), as well as matched electronic properties with multiple charge transfer processes.

Introduction

Organic and inorganic hybrid perovskite solar cells (PSCs) have attracted a lot of attention due to their broad absorption range, tunable optical bandgap, high charge carrier mobility, long charge carrier diffusion length and low-cost solution processability.[1–18] According to device architecture, PSCs can be roughly divided into inverted p–i–n and conventional n–i–p types. Generally, some advantages can be observed in inverted PSCs, including better ambient stability,[19–23] a smaller hysteresis effect,[23–26] and so on. In photovoltaic processes, the electron transport layer plays a key role in electron extraction from the perovskite layer and electron injection to the cathode. Fullerene and its derivatives, for instance, C_{60} and [6,6]-phenyl-C_{61}-butyric acid methyl ester ($PC_{61}BM$), are widely applied as electron transport materials (ETMs) owing to the aligned energy level, solution processability and high electron mobility.[27–34] However, their commercialization has been immensely limited due to their low water-resistant ability, unadjustable energy level, expensive commercial sources and undesirable film morphology. Alternatively, some non-fullerene electron transport materials with high electron mobilities, tunable energy levels and uniform morphology were investigated.[35–42] Among them, perylene diimide (**PDI**) derivatives as electron-withdrawing and planar π-conjugated systems are classical organic semiconductors with high electron mobilities, excellent thermal stability and simplified synthesis routes.[43–47] Moreover, they can provide diimide groups to coordinate with the uncoordinated Pb^{2+}, passivating traps on the surface of perovskite crystal grains, thus leading to the enhancement of conversion efficiency and device stability.[20,48–50] However, the planar structure of the **PDI** moiety always results in face-to-face stacking at the aggregated states, which may cause poor solubility and undesirable film morphology in some cases. Thus, the optimization of the molecular arrangement of **PDI** derivatives is essential, which can be conducted by adjustable molecular configurations, coupled with the tunable intramolecular charge transfer processes.[51–54] Various twisted building blocks, including tetraphenylethylene,[14] spiro-[fluorene-9,9′-xanthene],[55] [1,1′-bipyrrole]-2,2′,5,5′-tetraone,[56] phenothiazine 5,5-dioxide,[57] and so on, have been incorporated as the core units to modulate the interactions of **PDI** moieties at aggregated states. However, the conversion efficiencies of PSCs with **PDI**-based molecules as ETMs are still below 20%, which needed to be further enhanced by optimizing molecular configurations and electronic properties. Recently, the combination of electron donor (D) and electron acceptor (A) moieties into the conjugated systems has been proved as an efficient strategy due to their high charge mobility with the self-doping effect, which is mainly related to the strong intramolecular charge transfer (ICT) and strong dipole–dipole interactions.[58–62]

In consideration of these factors, an A–D–A type molecule of DiPDI-TPA (**DPT**) with triphenylamine (TPA) as the electron

[a] Hubei Key Lab on Organic and Polymeric Opto-Electronic Materials, Department of Chemistry, Wuhan University, Wuhan 430072, China. E-mail: liqianqian@whu.edu.cn, lizhen@whu.edu.cn
[b] Chongqing Key Laboratory for Advanced Materials and Technologies of Clean Energy, School of Materials & Energy, Southwest University, Chongqing 400715, P. R. China. E-mail: lnzhu@swu.edu.cn
[c] Institute of Molecular Aggregation Science, Tianjin University, Tianjin 300072, China

† Electronic supplementary information (ESI) available. See DOI: 10.1039/d1tc04176b
‡ These authors contributed equally.

donor and **PDI** as the electron acceptor has been designed and synthesized as the electron-transport material. The twisted TPA core can avoid the unfavorable stacking mode of the **PDI** moiety. Also, the rational combination of D and A moieties resulted in desirable structures for charge extraction and transport owing to the self-doping effect and built-in potential enhanced by the high dipole moment. A root mean square (RMS) roughness of 4.88 nm and a high electron mobility of 8.23×10^{-4} cm^2 V^{-1} s^{-1} were achieved in the **DPT** film, while those of 5.81 nm and 6.01×10^{-4} cm^2 V^{-1} s^{-1} for the $PC_{61}BM$ film as the reference, respectively. Furthermore, efficient electron extraction and inhibition of charge recombination at the perovskite/**DPT** interface can be achieved in PSC devices. Consequently, the highest power conversion efficiency (PCE) of 20.07% was achieved in the PSC with **DPT** as the ETM, while that of 18.38% in the reference PSC based on $PC_{61}BM$. Also, low hysteresis and great stability have been obtained for the optimized aggregate morphology.

Results and discussion

The target molecule **DPT** (Fig. 1) was synthesized by a Suzuki reaction between **PDI-Br** and **TPA-2Bpin** (Scheme S1, ESI†) and characterized by ^{1}H NMR, ^{13}C NMR, and HRMS spectroscopy and elemental analysis (Fig. S1 and S2, ESI†).

The UV-Vis absorption spectrum of **DPT** in dilute dichloromethane solution (1.0 μM) exhibited three peaks at 313 nm, 485 nm and 516 nm (Fig. 2a), which could be attributed to the π–π* transition and ICT process. Once the **DPT** molecules aggregated into a thin film, the absorption spectrum became broader. The photoluminescence spectra red-shifted about 130 nm from dilute solution to the film state, mainly due to the possible intermolecular interactions and planarity of molecular configuration at the aggregated state. The energy levels of the **DPT** film were calculated by ultraviolet photoelectron spectroscopy (UPS) and UV-Vis absorption spectroscopy (Fig. 2a and Fig. S3, ESI†), the results of which matched well with those for the perovskite layer. In detail, the lower LUMO energy level of −4.0 eV can favor electron extraction, and the deeper HOMO energy level of −5.7 eV benefits hole blocking.

The molecular conformation and orbital distribution of **DPT** were optimized by density functional theory (DFT) calculations

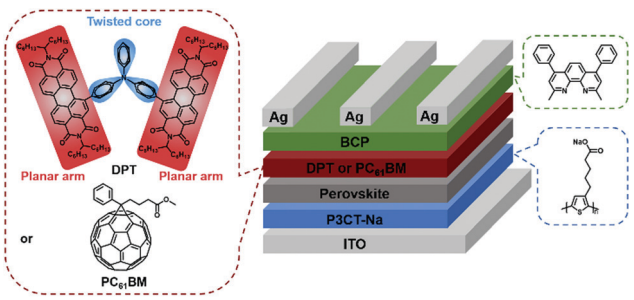

Fig. 1 The components and device architecture of an inverted PSC, in which **DPT** or $PC_{61}BM$ acted as the electron transport material.

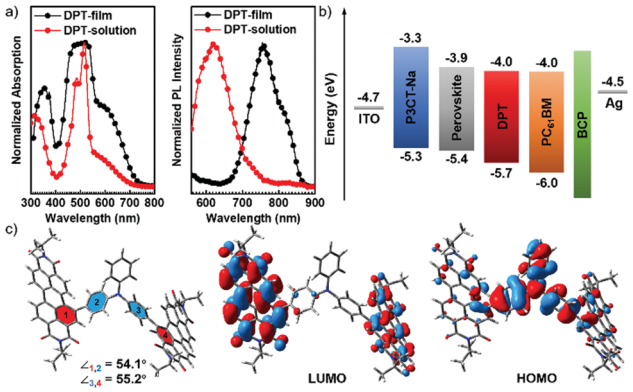

Fig. 2 (a) UV-Vis absorption and photoluminescence spectra of **DPT** in DCM solution (1.0 μM) and in the film state. (b) Energy level alignments of PSCs. (c) Optimized molecular configurations and LUMO and HOMO distributions of **DPT**.

at the B3LYP/6-31G(d) level (Fig. 2c).[63] It is found that **DPT** exhibits a twisted conformation with dihedral angles of 54.1° and 55.2°, defined by the adjacent phenyl moieties in TPA and **PDI**, respectively. The separated LUMO and HOMO distributions on the D or A moiety are obtained, favoring the electron transport process in the film and electron extraction from the perovskite layer. Furthermore, the role of twisted molecular conformation of **DPT** in molecular packing has been investigated, while **PDI** is employed as the reference, which is demonstrated by their photoluminescence spectra under different conditions (Fig. S8, ESI†). With the formation of molecular aggregates by the increased concentrations (1–100%, wt%) of **DPT** and **PDI** in a poly(methyl methacrylate) (PMMA) film gradually, their emission peaks and intensities exhibited various trends for their different molecular conformations. For **PDI** with an almost planar structure, a large shift of 85 nm with decreased intensities can be observed, indicating the strong π–π interactions at aggregated states. However, a small shift of 28 nm with increased intensities can be detected for **DPT**, which suggested the efficient suppression of π–π interactions with the quenching effect by the twisted molecular conformations. It is beneficial to the formation of a smooth film with uniform coverage, which can be further confirmed by AFM imaging.

The inverted p–i–n device was fabricated with the architecture of ITO/P3CT-Na/perovskite/ETL/BCP/Ag, while the ETL was formed by spin-coating of **DPT** or $PC_{61}BM$ solution. The **DPT**-based PSC exhibited excellent photovoltaic performance with a PCE of 19.23 ± 0.52%, a J_{SC} of 22.09 ± 0.21 mA cm^{-2}, a V_{OC} of 1.10 ± 0.01 V and a fill factor (FF) of 79.3 ± 1.4% (Fig. 3c and Fig. S4, Table S1, ESI†).

The concentrations of **DPT** solution for the fabrication process were tuned from 8 mg mL^{-1} to 15 mg mL^{-1}, and the thickness of the ETL increased gradually from 28.7 nm to 53.2 nm (Table S2, ESI†). Normally, the thinner film may result in incomplete coverage, leading to an unfavorable contact between the perovskite layer and cathode, while the thicker one usually induces an increase of charge transfer resistance.

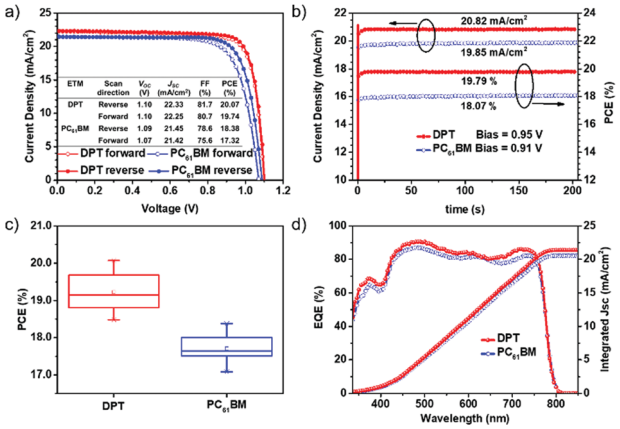

Fig. 3 (a) J–V curves of the PSCs with **DPT** and $PC_{61}BM$ as ETMs. (b) Stabilized photocurrent densities and efficiencies of PSCs with **DPT** and $PC_{61}BM$ as ETMs. (c) PCE distribution statistics of PSCs with **DPT** and $PC_{61}BM$ as ETMs. (d) EQE spectra and the integrated J_{SC} values for PSCs with **DPT** and $PC_{61}BM$ as ETMs.

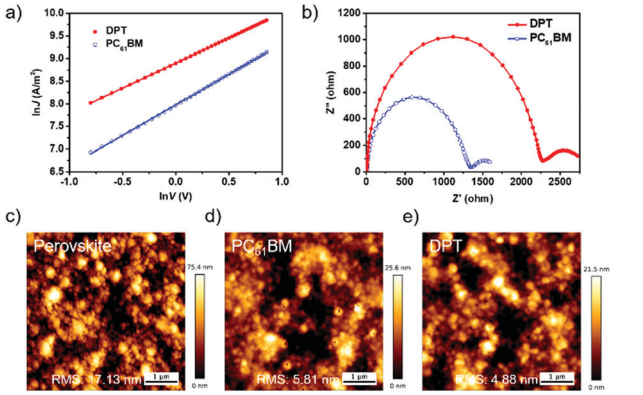

Fig. 4 (a) SCLC characteristics obtained from the electron-only devices. (b) Nyquist plots of PSCs with **DPT** and $PC_{61}BM$ measured at an applied bias of 1.0 V in the dark. Atomic force microscopy (AFM) images of (c) the perovskite film and that covered by (d) $PC_{61}BM$ and (e) **DPT**, respectively.

Therefore, the highest PCE of 20.07% was achieved at the proper thickness of 44.6 nm with a concentration of 12 mg mL^{-1}, for the balance of the coverage on the perovskite layer and charge transfer resistance of the ETL (Table S2, ESI†), which is also the highest one among all the reported **PDI**-based molecules as ETMs, to the best of our knowledge (Table S3 and Fig. S5, ESI†). The reference PSC with $PC_{61}BM$ exhibited a PCE of 17.71 ± 0.36%, a J_{SC} of 21.25 ± 0.19 mA cm^{-2}, a V_{OC} of 1.08 ± 0.01 V and a FF of 76.9 ± 1.1%. The better performance of PSCs with **DPT**, especially the increased J_{SC} and FF values, indicated the efficient electron extraction and electron transport capacity. Furthermore, negligible hysteresis effect can be observed in the **DPT**-based PSC (Fig. 3a), and PCEs of 20.07% and 19.74% were obtained in reverse and forward scans, respectively. The low hysteresis can be attributed to the suppression of ion migration in the perovskite layer and charge accumulation at the interface between the perovskite layer and ETM.

In external quantum efficiency (EQE) spectra, high responses approaching 90% were obtained in the region from 400 nm to 800 nm (Fig. 3d), and the integrated J_{SC} value (21.40 mA cm^{-2}) matched well with the J–V curve. The stabilized photocurrent densities and efficiencies (Fig. 3b) were measured at the maximum power output points (with a bias of 0.95 V for the **DPT**-based device and 0.91 V for the $PC_{61}BM$-based device). Apparently, a higher stabilized photocurrent density of 20.82 mA cm^{-2} and a stabilized efficiency of 19.79% were obtained in the **DPT**-based device, compared to those of 19.85 mA cm^{-2} and 18.07% in the $PC_{61}BM$-based one, respectively. These are consistent with the J–V curves, further confirming the superiority of **DPT** as the ETM.

To investigate the charge-carrier transport properties, steady-state space charge-limited currents (SCLCs) were measured in the electron-only devices with the ITO/ZnO/**DPT** or $PC_{61}BM$/BCP/Ag structure (Fig. 4a). The electron mobility of the **DPT** film is 8.23 × 10^{-4} cm^2 V^{-1} s^{-1}, which is obviously higher than that of $PC_{61}BM$ (6.01 × 10^{-4} cm^2 V^{-1} s^{-1}), thus contributing to the efficient electron transport process.

Furthermore, electrochemical impedance spectroscopy (EIS) was performed at a bias voltage of 1.0 V in the dark (Fig. 4b). Obviously, the recombination resistance (R_{rec}) of the **DPT**-based device is larger than that of the $PC_{61}BM$-based one. The surface morphology was measured by atomic force microscopy (AFM) (Fig. 4c–e). The RMS roughness value of the bare perovskite is 17.13 nm, while it can be roughly reduced to 5.81 nm or 4.88 nm by spin-coating of $PC_{61}BM$ or **DPT**, respectively. The smoother film morphology of the **DPT**-based one can favor the better contact between the perovskite and Ag cathode.

Steady-state and time-resolved photoluminescence spectra of the ITO/perovskite, ITO/perovskite/**DPT** and ITO/perovskite/$PC_{61}BM$ were measured to evaluate the charge extraction properties of **DPT** as the ETM (Fig. 5a and b). The photoluminescence of the perovskite can be sharply quenched after the spin-coating of **DPT** or $PC_{61}BM$, and the PL lifetime of the bare perovskite (120.4 ns) decreased rapidly to 56.9 ns by the addition of **DPT**, while that caused by $PC_{61}BM$ is 57.6 ns. The shorter lifetime of the **DPT**-coated perovskite confirmed the more effective electron extraction of **DPT** as the ETM. Furthermore, electron extraction and charge recombination of PSCs were investigated by transient photovoltage (TPV) and transient photocurrent (TPC) measurements. The longer decay time of **DPT** also suggested the efficient inhibition of charge recombination at the interface. According to the relationship between charge transfer time (τ_j), photocurrent decay time (τ_c) and photovoltage decay time (τ_v) as $1/\tau_j = 1/\tau_c - 1/\tau_v$,[45,64,65] the **DPT**-based PSC exhibits shorter τ_c (2.1 μs) and longer τ_v (0.19 ms), compared to those of the $PC_{61}BM$-based device (3.0 μs and 0.12 ms), confirming the faster charge transfer in the **DPT**-based device. This can be ascribed to the effective electron extraction and faster electron transport in the **DPT** film.

Desirable storage stability of PSCs can also be achieved (Fig. S6, ESI†) by the **DPT** based device, which retained 94.0% of the initial PCE after storing under an atmosphere of nitrogen

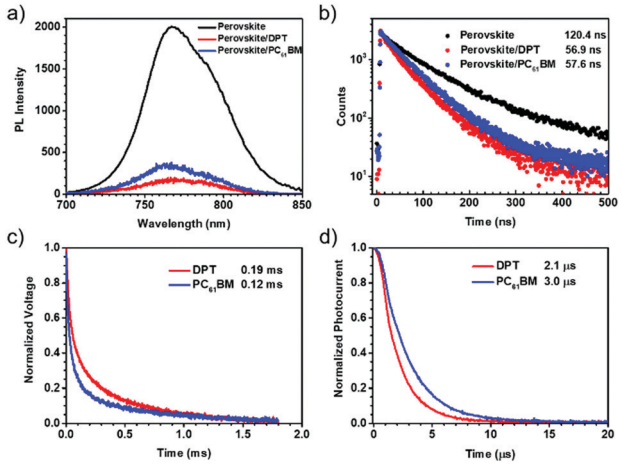

Fig. 5 (a) Steady-state and (b) time-resolved PL spectra of the perovskite, perovskite/**DPT** and perovskite/$PC_{61}BM$. (c) Transient photovoltage (TPV) and (d) transient photocurrent (TPC) measurement of the devices with **DPT** and $PC_{61}BM$ as ETMs.

for 30 days. The $PC_{61}BM$ based device retained 91.6% under the same conditions. The better stability of the **DPT** based device can be ascribed to the stronger hydrophobicity of **DPT**, which can be further confirmed by the higher water contact angle on the surface of perovskite/**DPT** (92.6°) than that on perovskite/$PC_{61}BM$ (83.6°) (Fig. S7, ESI†).

Conclusions

In conclusion, we developed a **PDI** derivative (**DPT**) with an A–D–A structure as the ETM in inverted PSCs by introduction of a twisted electron donor, TPA, as the linkage unit of two **PDI** fragments. The desirable morphology, electron mobility, and electron extraction, together with the efficient suppression of charge recombination, were obtained, as confirmed by AFM, SCLC, steady-state and time-resolved PL spectra, and EIS, TPV and TPC measurements, respectively. Accordingly, a high PCE of 20.07% was achieved by the **DPT**-based PSC, which is superior to that of the $PC_{61}BM$-based one (18.38%). Also, **DPT** as the ETM can reduce the possible hysteresis and stabilize the PSC device by the efficient charge extraction and hydrophobic properties. It proved an efficient strategy to design excellent ETMs by adjustment of molecular configurations and electronic properties, which can promote the development of PSCs with enhanced conversion efficiencies and storage stability simultaneously.

Experimental section

Materials

Most of the materials for device fabrication were purchased from commercial suppliers and used without further purification, including P3CT (Rieke Metals), PbI_2 (p-OLED, >99.99%), $PbCl_2$ (p-OLED, >99.99%), MAI (p-OLED, ≥99.5%), $PC_{61}BM$ (p-OLED), BCP (p-OLED), DMF (Sigma-Aldrich, 99.8%), DMSO (Sigma-Aldrich, 99.8%) and CB (Sigma-Aldrich, 99.8%). Toluene (Tol) and tetrahydrofuran (THF) were distilled from the sodium potassium alloy under an atmosphere of argon. 1,4-Dioxane was bubbled with nitrogen flow. Chemical reagents and solvents were obtained commercially and used without further purification.

Synthesis of TPA-2Br. Under an atmosphere of nitrogen, 4-bromoiodobenzene (14.15 g, 50 mmol), 1,10-phenanthroline hydrate (0.59 g, 4 mmol), aniline (1.38 mL, 20 mmol), CuI (0.57 g, 4 mmol), KOH (6.66 g, 16 mmol) and toluene (40 mL) were stirred at 120 °C for 12 hours. After cooling to room temperature, water was added and the mixture was extracted with dichloromethane several times. The combined organic layers were dried with anhydrous Na_2SO_4 and concentrated by rotary evaporation. The crude product was purified by column chromatography on silica gel using petroleum ether as the eluent. White solid (6.31 g, 78.3%). ^{1}H NMR (400 MHz, chloroform-*d*) δ (ppm): 7.34–7.32 (d, J = 8.8 Hz, 4H), 7.28–7.24 (t, J = 7.8 Hz, 2H), 7.07–7.04 (m, 3H), 6.94–6.92 (d, J = 8.8 Hz, 4H).

Synthesis of TPA-2Bpin. Under an atmosphere of nitrogen, **TPA-2Br** (1.21 g, 3 mmol), bis(pinacolato)diboron (1.90 mg, 7.5 mmol), KOAc (1.77 g, 18 mmol), $Pd(dppf)_2Cl_2$ (73.5 mg, 0.09 mmol), and 1,4-dioxane (15 mL) were stirred at 120 °C for 12 hours. After cooling to room temperature, water was added and the mixture was extracted with dichloromethane several times. The combined organic layers were dried with anhydrous Na_2SO_4 and concentrated by rotary evaporation. The crude product was purified by column chromatography on silica gel using dichloromethane/petroleum (1 : 1, v/v) ether as the eluent and recrystallization in methanol and hexane. Colourless crystals (1.30 g, 86.9%). ^{1}H NMR (400 MHz, dichloromethane-d_2) δ (ppm): 7.64–7.61 (d, J = 8.5 Hz, 4H), 7.31–7.27 (t, J = 7.9 Hz, 2H), 7.12–7.08 (m, 3H), 7.04–7.02 (d, J = 8.5 Hz, 4H), 1.32 (s, 24H).

Synthesis of PDI. Under an atmosphere of nitrogen, 3,4,9,10-perylenetetracarboxylic dianhydride (3.92 g, 10 mmol) and tridecan-7-amine (4.99 g, 25 mmol) in *N*-methyl pyrrolidone (150 mL) were stirred at 90 °C for 24 hours. After cooling to room temperature, the mixture was then poured into water and extracted with dichloromethane several times. The combined organic layers were dried with anhydrous Na_2SO_4 and concentrated by rotary evaporation. The crude product was purified by column chromatography on silica gel using dichloromethane/petroleum ether (1 : 4, v/v) as the eluent. Orange solid (6.59 g, 87.3%). ^{1}H NMR (400 MHz, chloroform-*d*) δ (ppm): 8.68–8.62 (m, 8H), 5.22–5.15 (m, 2H), 2.30–2.20 (m, 4H), 1.91–1.82 (m, 4H), 1.36–1.21 (m, 32H), 0.84–0.81 (t, J = 6.9 Hz, 12H).

Synthesis of PDI-Br. In a dichloromethane solution of **PDI** (5.29 g, 7 mmol), Br_2 (18.2 mL, 350 mmol) was added. The mixture was stirred at 40 °C for 16 hours. After cooling to room temperature, a saturated aqueous solution of Na_2SO_3 was added and extracted with dichloromethane several times. The combined organic layers were dried with anhydrous Na_2SO_4 and concentrated by rotary evaporation. The crude product was purified by column chromatography on silica gel using dichloromethane/petroleum ether (1 : 4, v/v) as the eluent. Red solid (3.40 g, 58.3%). ^{1}H NMR (400 MHz, chloroform-*d*) δ (ppm):

9.80–9.78 (d, J = 8.3 Hz, 1H), 8.92 (s, 1H), 8.70 (s, 3H), 8.63–8.61 (m, 2H), 5.23–5.13 (m, 2H), 2.30–2.19 (m, 4H), 1.91–1.81 (m, 4H), 1.37–1.20 (m, 32H), 0.84–0.81 (m, 12H).

Synthesis of DPT. Under an atmosphere of nitrogen, **PDI-Br** (2.08 g, 2.5 mmol), **TPA-2Bpin** (0.50 mg, 1.0 mmol), K_2CO_3 (0.55 mg, 4.0 mmol) and $Pd(PPh_3)_4$ (0.15 g, 0.13 mmol) were dissolved in the solvent of THF (10 mL) and H_2O (2 mL). The mixture was stirred at 70 °C for 12 hours. After cooling to room temperature, water was added and the mixture was extracted with dichloromethane several times. The organic layers were dried with anhydrous Na_2SO_4 and concentrated by rotary evaporation. The crude product was purified by column chromatography on silica gel using dichloromethane/petroleum ether (2 : 1, v/v) as the eluent. Purple solid (864 mg, 49.33%). ^{1}H NMR (400 MHz, dichloromethane-d_2) δ (ppm): 8.63–8.58 (m, 10H), 8.24–8.19 (m, 2H), 8.16–8.14 (d, J = 8.2 Hz, 2H), 7.48–7.43 (m, 6H), 7.37–7.32 (m, 6H), 7.22–7.18 (t, J = 7.4 Hz, 1H), 5.21–5.09 (m, 4H), 2.29–2.17 (m, 8H), 1.87–1.77 (m, 8H), 1.31–1.18 (m, 64H), 0.84–0.76 (m, 24H). ^{13}C NMR (100 MHz, dichloromethane-d_2) δ (ppm): 164.54, 163.38, 147.75, 146.94, 141.34, 136.85, 136.22, 134.94, 134.66, 134.40, 132.33, 131.28, 130.54, 130.19, 129.76, 129.67, 129.18, 128.40, 128.10, 127.59, 125.75, 125.17, 124.33, 123.78, 123.54, 123.02, 122.59, 122.17, 32.32, 32.28, 31.80, 31.74, 29.25, 29.20, 26.89, 26.83, 22.62, 22.58, 13.84, 13.81. MS (HRMS): calcd for ($C_{118}H_{135}N_5O_8$), 1751.4050; found, 1751.1130. Anal. calcd for $C_{118}H_{135}N_5O_8$: C, 80.92; H, 7.77; N, 4.00. Found: C, 80.70; H, 7.57; N, 3.92.

Device fabrication

The indium tin oxide (ITO) glass substrates were washed by sonication using detergent, deionized water, as well as ethanol sequentially, and then dried using nitrogen flow. The hole transport layer P3CT-Na (1 mg mL^{-1} in H_2O) was formed on ITO substrates by spin coating at 4000 rpm for 60 s, followed by annealing at 140 °C for 30 min. Then the samples were transferred into a N_2-filled glovebox. $CH_3NH_3PbI_{3-x}Cl_x$ precursor solution (1.26 M PbI_2, 0.14 M $PbCl_2$ and 1.4 M MAI in a DMF : DMSO mixed solution with a v/v of 9 : 1, stirred overnight at room temperature) was spin-coated on P3CT-Na substrates at 400 rpm for 3 s and 4000 rpm for 30 s. During the spin coating process, chlorobenzene (150 μL) was dripped directly on the substrates after being spin-coated for 11 s, followed by annealing at 50 °C for 2 min and 85 °C for 25 min. Then, $PC_{61}BM$ solution (20 mg mL^{-1}) or **DPT** solution (8–15 mg mL^{-1}) in chlorobenzene was spin-coated onto the perovskite layer. BCP (6 nm) was evaporated under a high vacuum (10^{-5} Pa) on top of the ITO/P3CT-Na/perovskite/ETL substrate. Finally, a 100 nm thick Ag electrode was deposited through a shadow mask. The active area of the device is 0.0625 cm^2.

Characterization

^{1}H and ^{13}C NMR spectra were recorded on a Bruker Avance III HD 400 MHz using tetramethylsilane (TMS; δ = 0 ppm) as the internal standard. High-resolution mass spectra were measured on an LTQ-Orbitrap Elite high-resolution mass spectrometer (Thermo Fisher Scientific, Waltham, USA). Elemental analyses were performed using a PerkinElmer microanalyzer. UV-vis absorption spectra were measured on a Shimadzu UV-2501 recording spectrophotometer. Steady-state and time-resolved PL spectra were measured using an FLS980 spectrometer. The UPS of the **DPT** film was measured using a Thermo ESCALAB XI+. Atomic force microscopy (AFM) measurements were performed with a Nano Wizard atomic force microscope (JPK Inc. Germany) in the Qi mode to observe the surface morphology of the corresponding films on ITO glass substrates. The electron mobilities were measured by the SCLC method and the Mott–Gurney law based on electron-only devices with the ITO/ZnO/**DPT** or $PC_{61}BM$/BCP/Ag structure. The current–voltage (J–V) curves were measured using a Keithley 2400 in conjunction with a Newport solar simulator (94043A) under 100 mW cm^{-2} (AM 1.5G) simulated sunlight. Electrochemical impedance spectroscopy (EIS) was measured using a CHI660. The external quantum efficiency (EQE) was calculated from the photocurrent measurement under monochromatic illumination at different wavelengths with a 150 W xenon lamp and a monochromator. Transient photocurrent (TPC) and transient photovoltage (TPV) were recorded using a ZAHNER® MESSSYSTEME (instrument model: PP211) with a light source (LS530). The thickness of the ETL was measured using an ET150 Microfigure Measuring Instrument Model (Kosaka Laboratory Ltd).

Author contributions

Q. L. and Z. L. conceived the project. Y. F. synthesized the materials and performed the measurements of UV-Vis, steady-state and time-resolved PL spectra, as well as AFM, UPS and relative purity identification. F. W. and L. Z. performed the device fabrication, J–V curve measurements, stabilized photocurrent densities and efficiency measurements, EQE measurements, Nyquist plot measurements, SCLC measurements, TPV as well as TPC measurements and stability test of the devices. F. L. performed the synthetic experiments. M. H. performed the theoretical calculations. K. C. performed the AFM measurements. Q. L. and Z. L. discussed and revised the manuscript. All the authors approved the manuscript.

Conflicts of interest

There are no conflicts to declare.

Acknowledgements

We are grateful to the National Natural Science Foundation of China (no. 21875174 and 21734007), Excellent Youth Foundation of Hubei Scientific Committee (2020CFA084), and the Fundamental Research Funds for the Central Universities (2042020kf0200) and Wuhan City (2019010701011412) for financial support.

Notes and references

1 D. Shi, V. Adinolfi, R. Comin, M. Yuan, E. Alarousu, A. Buin, Y. Chen, S. Hoogland, A. Rothenberger, K. Katsiev, Y. Losovyj, X. Zhang, P. A. Dowben, O. F. Mohammed, E. H. Sargent and O. M. Bakr, *Science*, 2015, **347**, 519–522.
2 W. Nie, H. Tsai, R. Asadpour, J.-C. Blancon, A. J. Neukirch, G. Gupta, J. J. Crochet, M. Chhowalla, S. Tretiak, M. A. Alam, H.-L. Wang and A. D. Mohite, *Science*, 2015, **347**, 522–525.
3 M. A. Green, A. Ho-Baillie and H. J. Snaith, *Nat. Photonics*, 2014, **8**, 506–514.
4 D. Yang, R. Yang, X. Ren, X. Zhu, Z. Yang, C. Li and S. Liu, *Adv. Mater.*, 2016, **28**, 5206–5213.
5 C. Wehrenfennig, M. Liu, H. J. Snaith, M. B. Johnston and L. M. Herz, *Energy Environ. Sci.*, 2014, **7**, 2269–2275.
6 Z. Xiao, Q. Dong, C. Bi, Y. Shao, Y. Yuan and J. Huang, *Adv. Mater.*, 2014, **26**, 6503–6509.
7 Q. Dong, Y. Fang, Y. Shao, P. Mulligan, J. Qiu, L. Cao and J. Huang, *Science*, 2015, **347**, 967–970.
8 S. D. Stranks, G. E. Eperon, G. Grancini, C. Menelaou, M. J. P. Alcocer, T. Leijtens, L. M. Herz, A. Petrozza and H. J. Snaith, *Science*, 2013, **342**, 341–344.
9 Q. Lin, A. Armin, R. C. R. Nagiri, P. L. Burn and P. Meredith, *Nat. Photonics*, 2015, **9**, 106–112.
10 J.-P. Correa-Baena, M. Saliba, T. Buonassisi, M. Grätzel, A. Abate, W. Tress and A. Hagfeldt, *Science*, 2017, **358**, 739–744.
11 D. Liu, W. Zhou, H. Tang, P. Fu and Z. Ning, *Sci. China: Chem.*, 2018, **61**, 1278–1284.
12 K. Kobayashi, H. Hasegawa, Y. Takahashi, J. Harada and T. Inabe, *Mater. Chem. Front.*, 2018, **2**, 1291–1295.
13 N. Wang, W. Liu and Q. Zhang, *Small Methods*, 2018, **2**, 1700380.
14 F. Liu, S. Bi, X. Wang, X. Leng, M. Han, B. Xue, Q. Li, H. Zhou and Z. Li, *Sci. China: Chem.*, 2019, **6**, 739–745.
15 J.-H. Chen, S.-D. Yang, W.-Q. Liu, W.-F. Fu and H.-Z. Chen, *Chin. J. Polym. Sci.*, 2017, **2**, 309–316.
16 D. Ti, K. Gao, Z.-P. Zhang and L.-T. Qu, *Chin. J. Polym. Sci.*, 2020, **38**, 449–458.
17 H. Chen, Y. Chen, T. Zhang, X. Liu, X. Wang and Y. Zhao, *Small Struct.*, 2021, **2**, 2000130.
18 P. Chen, Y. Bai and L. Wang, *Small Struct.*, 2021, **2**, 2000050.
19 K. Jiang, F. Wu, H. Yu, Y. Yao, G. Zhang, L. Zhu and H. Yan, *J. Mater. Chem. A*, 2018, **6**, 16868–16873.
20 Z. Luo, F. Wu, T. Zhang, X. Zeng, Y. Xiao, T. Liu, C. Zhong, X. Lu, L. Zhu, S. Yang and C. Yang, *Angew. Chem., Int. Ed.*, 2019, **58**, 8520–8525.
21 D. Zou, F. Yang, Q. Zhuang, M. Zhu, Y. Chen, G. You, Z. Lin, H. Zhen and Q. Ling, *ChemSusChem*, 2019, **12**, 1155–1161.
22 F. Liu, F. Wu, W. Ling, Z. Tu, J. Zhang, Z. Wei, L. Zhu, Q. Li and Z. Li, *ACS Energy Lett.*, 2019, **4**, 2514–2521.
23 J. H. Heo, S.-C. Lee, S.-K. Jung, O.-P. Kwon and S. H. Im, *J. Mater. Chem. A*, 2017, **5**, 20615–20622.
24 F. Wu, W. Gao, H. Yu, L. Zhu, L. Li and C. Yang, *J. Mater. Chem. A*, 2018, **6**, 4443–4448.
25 Z. Hu, G. Tang, J. Miao, T. Fu, T. Li, Q. Tai, H. Meng and F. Yan, *Adv. Funct. Mater.*, 2020, **30**, 2001073.
26 X. Liu, X. Li, Y. Zou, H. Liu, L. Wang, J. Fang and C. Yang, *J. Mater. Chem. A*, 2019, **7**, 3336–3343.
27 B. Li, J. Zhen, Y. Wan, X. Lei, Q. Liu, Y. Liu, L. Jia, X. Wu, H. Zeng, W. Zhang, G.-W. Wang, M. Chen and S. Yang, *ACS Appl. Mater. Interfaces*, 2018, **10**, 32471–32482.
28 J. Chang, Y.-C. Wang, C. Song, L. Zhu, Q. Guo and J. Fang, *J. Mater. Chem. C*, 2018, **6**, 6982–6987.
29 C. Tian, E. Castro, T. Wang, G. Betancourt-Solis, G. Rodriguez and L. Echegoyen, *ACS Appl. Mater. Interfaces*, 2016, **8**, 31426–31432.
30 L. Meng, J. You, T.-F. Guo and Y. Yang, *Acc. Chem. Res.*, 2016, **49**, 155–165.
31 P.-W. Liang, C.-C. Chueh, S. T. Williams and A. K.-Y. Jen, *Adv. Energy Mater.*, 2015, **5**, 1402321.
32 X. Liu, W. Jiao, M. Lei, Y. Zhou, B. Song and Y. Li, *J. Mater. Chem. A*, 2015, **3**, 9278–9284.
33 X. Sun, Z. Li, X. Yu, X. Wu, C. Zhong, D. Liu, D. Lei, A. K.-Y. Jen, Z. Li and Z. Zhu, *Angew. Chem., Int. Ed.*, 2021, **60**, 7227.
34 X. Yu, Z. Li, X. Sun, C. Zhong, Z. Zhu, Z. Li and A. K.-Y. Jen, *Nano Energy*, 2021, **82**, 105701.
35 C. Song, X. Li, Y. Wang, S. Fu, L. Wan, S. Liu, W. Zhang, W. Song and J. Fang, *J. Mater. Chem. A*, 2019, **7**, 19881–19888.
36 W. Chen, A. A. Said, Z. Wang, Y. Zhou, W. Liu, W.-B. Gao, M. Liu and Q. Zhang, *ACS Appl. Energy Mater.*, 2019, **2**, 5716–5723.
37 S.-K. Jung, J. H. Heo, B. M. Oh, J. B. Lee, S.-H. Park, W. Yoon, Y. Song, H. Yun, J. H. Kim, S. H. Im and O.-P. Kwon, *Adv. Funct. Mater.*, 2020, **30**, 1905951.
38 S.-K. Jung, J. H. Heo, D. W. Lee, S.-C. Lee, S.-H. Lee, W. Yoon, H. Yun, S. H. Im, J. H. Kim and O.-P. Kwon, *Adv. Funct. Mater.*, 2018, **28**, 1800346.
39 R. Zhu, Q.-S. Li and Z.-S. Li, *J. Mater. Chem. A*, 2019, **7**, 16304–16312.
40 N. Wang, K. Zhao, T. Ding, W. Liu, A. S. Ahmed, Z. Wang, M. Tian, X. W. Sun and Q. Zhang, *Adv. Energy Mater.*, 2017, **7**, 1700522.
41 D. Zhao, Z. Zhu, M.-Y. Kuo, C.-C. Chueh and A. K.-Y. Jen, *Angew. Chem., Int. Ed.*, 2016, **55**, 8999–9003.
42 Y. Gao, Y. Wu, Y. Liu, M. Lu, L. Yang, Y. Wang, W. W. Yu, X. Bai, Y. Zhang and Q. Dai, *Nanoscale Horiz.*, 2020, **5**, 1574–1585.
43 E. Castro, T. J. Sisto, E. L. Romero, F. Liu, S. R. Peurifoy, J. Wang, X. Zhu, C. Nuckolls and L. Echegoyen, *Angew. Chem., Int. Ed.*, 2017, **56**, 14648–14652.
44 R. Wang, K. Jiang, H. Yu, F. Wu, L. Zhu and H. Yan, *Mater. Chem. Front.*, 2019, **3**, 2137–2142.
45 J.-l. Wu, W.-K. Huang, Y.-C. Chang, B.-C. Tsai, Y.-C. Hsiao, C.-Y. Chang, C.-T. Chen and C.-T. Chen, *J. Mater. Chem. A*, 2017, **5**, 12811–12821.
46 F. Ye, D. Zhang, X. Xu, H. Guo, S. Liu, S. Zhang, Y. Wu and W.-H. Zhu, *Sol. RRL*, 2021, **5**, 2000736.
47 Z. Liu, Y. Wu, Q. Zhang and X. Gao, *J. Mater. Chem. A*, 2016, **4**, 17604–17622.

48 H. Wang, F. Yang, N. Li, J. Song, J. Qu, S. Hayase and W.-Y. Wong, *Chem. Eng. J.*, 2020, **392**, 123677.
49 F. Wu, Z. Luo, L. Zhu, C. Chen, H. Lu, Z. Chen, J. Tang and C. Yang, *J. Mater. Chem. A*, 2019, **7**, 21176–21181.
50 H. Wang, F. Yang, Y. Xiang, S. Ye, X. Peng, J. Song, J. Qu and W.-Y. Wong, *J. Mater. Chem. A*, 2019, **7**, 24191–24198.
51 Y. Liu, C. Mu, K. Jiang, J. Zhao, Y. Li, L. Zhang, Z. Li, J. Y. L. Lai, H. Hu, T. Ma, R. Hu, D. Yu, X. Huang, B. Z. Tang and H. Yan, *Adv. Mater.*, 2015, **27**, 1015–1020.
52 Y. Li, M. Han, W. Yang, J. Guo, K. Chang, J. Wang, J. Min, Q. Li and Z. Li, *Mater. Chem. Front.*, 2019, **3**, 1840–1848.
53 Q. Li and Z. Li, *Acc. Chem. Res.*, 2020, **53**, 962–973.
54 F. Liu, Q. Liao, J. Wang, Y. Gong, Q. Dang, W. Ling, M. Han, Q. Li and Z. Li, *Sci. China: Chem.*, 2020, **63**, 1435–1442.
55 M. Cheng, Y. Li, P. Liu, F. Zhang, A. Hajian, H. Wang, J. Li, L. Wang, L. Kloo, X. Yang and L. Sun, *Sol. RRL*, 2017, **1**, 1700046.
56 P. Karuppuswamy, H.-C. Chen, P.-C. Wang, C.-P. Hsu, K.-T. Wong and C.-W. Chu, *ChemSusChem*, 2018, **11**, 415–423.
57 M. Zheng, Y. Miao, A. A. Syed, C. Chen, X. Yang, L. Ding, H. Li and M. Cheng, *J. Energy Chem.*, 2021, **56**, 374–382.
58 P. Xu, P. Liu, Y. Li, B. Xu, L. Kloo, L. Sun and Y. Hua, *ACS Appl. Mater. Interfaces*, 2018, **10**, 19697–19703.
59 Z. Gong, R. Wang, Y. Jiang, X. Kong, Y. Lin, Z. Xu, G. Zhou, J.-M. Liu, K. Kempa and J. Gao, *Org. Electron.*, 2021, **92**, 106102.
60 Y. Wang, W. Chen, L. Wang, B. Tu, T. Chen, B. Liu, K. Yang, C. W. Koh, X. Zhang, H. Sun, G. Chen, X. Feng, H. Y. Woo, A. B. Djurišić, Z. He and X. Guo, *Adv. Mater.*, 2019, **31**, 1902781.
61 Z. Li, Z. Zhu, C.-C. Chueh, S. B. Jo, J. Luo, S.-H. Jang and A. K.-Y. Jen, *J. Am. Chem. Soc.*, 2016, **138**, 11833–11839.
62 S. A. Ok, B. Jo, S. Somasundaram, H. J. Woo, D. W. Lee, Z. Li, B.-G. Kim, J. H. Kim, Y. J. Song, T. K. Ahn, S. Park and H. J. Park, *Nat. Commun.*, 2018, **9**, 4537.
63 M. J. Frisch, G. W. Trucks, H. B. Schlegel, G. E. Scuseria, M. A. Robb, J. R. Cheeseman, G. Scalmani, V. Barone, B. Mennucci, G. A. Petersson, H. Nakatsuji, M. Caricato, X. Li, H. P. Hratchian, A. F. Izmaylov, J. Bloino, G. Zheng, J. L. Sonnenberg, M. Hada, M. Ehara, K. Toyota, R. Fukuda, J. Hasegawa, M. Ishida, T. Nakajima, Y. Honda, O. Kitao, H. Nakai, T. Vreven, J. A. Montgomery, Jr., J. E. Peralta, F. Ogliaro, M. Bearpark, J. J. Heyd, E. Brothers, K. N. Kudin, V. N. Staroverov, T. Keith, R. Kobayashi, J. Normand, K. Raghavachari, A. Rendell, J. C. Burant, S. S. Iyengar, J. Tomasi, M. Cossi, N. Rega, J. M. Millam, M. Klene, J. E. Knox, J. B. Cross, V. Bakken, C. Adamo, J. Jaramillo, R. Gomperts, R. E. Stratmann, O. Yazyev, A. J. Austin, R. Cammi, C. Pomelli, J. W. Ochterski, R. L. Martin, K. Morokuma, V. G. Zakrzewski, G. A. Voth, P. Salvador, J. J. Dannenberg, S. Dapprich, A. D. Daniels, O. Farkas, J. B. Foresman, J. V. Ortiz, J. Cioslowski and D. J. Fox, *Gaussian 09, Revision D.01*, Gaussian, Inc., Wallingford CT, 2013.
64 K. Liu, S. Dai, F. Meng, J. Shi, Y. Li, J. Wu, Q. Meng and X. Zhan, *J. Mater. Chem. A*, 2017, **5**, 21414–21421.
65 J. Shi, D. Li, Y. Luo, H. Wu and Q. Meng, *Rev. Sci. Instrum.*, 2016, **87**, 123107.

